

Validation of Different Approaches to Coupled Electrodynamic – Structural Mechanical Simulation of Electromagnetic Forming*

M. Stiemer¹, M. Klocke², F. T. Suttmeier¹, H. Blum¹, A. Joswig², S. Kulig²

¹Chair of Scientific Computing, University of Dortmund

²Institute of Electrical Machines, Drivers and Power Electronics, University of Dortmund

Abstract

Electromagnetic forming (EF) is a high speed forming process in which strain rates of over $10^3 s^{-1}$ are achieved. The workpiece is deformed by the Lorentz force resulting from the interaction of a fast varying electro magnetic field with the eddy currents induced by the field in the workpiece. Within a research group (FOR 443) funded by the German Research Foundation (DFG) an object oriented simulation tool for this multi physical process has been developed (SOFAR), that can handle the fully coupled simulation in a single software environment. In this contribution, details of the algorithmic implementation of the electromagnetic side of the coupled model are discussed and validated. Basis of this validation are benchmark simulations developed for this purpose. In particular, the implementation of transient field computation for coupled problems within SOFAR is compared with an experienced FD-code (FELMEC) developed at the Institute of Electrical Machines, Drives and Power Electronics.

Keywords:

Modeling, Simulation, Electromagnetic Forming

1 Introduction

Electromagnetic forming (EF) is a dynamical forming process that is driven by the interaction of a pulsed magnetic field with eddy currents induced by the exciting field. The workpiece to be formed consists of good conducting material like copper or aluminum. A tool coil adjacent to the workpiece is excited by a fast time varying current. The resulting pulsed magnetic field diffuses into the work piece and induces eddy currents there. These eddy currents again in-

*This work is based on the results of the research group FOR 443. The authors wish to thank the Deutsche Forschungsgemeinschaft – DFG for its financial support.

interact with the exciting magnetic field which results in a material body force, e.g. the Lorentz force representing an additional supply of momentum that results in deformation. EF offers advantages over other forming methods such as increase in formability for certain kinds of materials, reduction in wrinkling, the ability to combine forming and assembly operations, reduced tool making costs etc.. Despite these advantages, its industrial application is concentrated on joining tubular semifinished material (see [1, 2]), whereas electromagnetic sheet metal forming (ESF) has not been developed to a point where it may be routinely used for industrial purposes yet. The determination of the optimal progression of the magnetic field strength including the design of tool coils and power supply devices requires still scientific research. Nevertheless, recent research activities [3, 4] have led to a precise description and process analysis of the free forming of aluminum sheet metal.

The above mentioned difficulties demonstrate the significance of reliable simulation tools for EF. However, these require a non linear coupling of a mechanical simulation considering the material's dependence on the strain rate with an electromagnetic one. Since the introduction of high speed computers in the late 80's, several different approaches to EF have been carried out (see [5, 6, 7, 8, 1, 2, 3, 9]). The simulation developed within the DFG research group FOR 443 is based on a general approach to the formulation of continuum thermodynamic models for a class of rate-dependent metallic engineering materials dynamically formed via strong magnetic fields due to Svendsen and Chanda [10, 11]. The validity of (a specialised form of) these models has been verified experimentally in Brosius et al. [12, 13]. The algorithmic formulation of the coupled model and its efficient numerical implementation has been carried out and discussed in [14]. As software environment the object oriented code SOFAR (**S**mall **O**bject oriented **F**inite-element-library for **A**pplication and **R**esearch) has been chosen [15]. Moreover, the mechanical side of the simulation has been validated by benchmark simulations in [16].

In the present contribution we discuss different algorithmic approaches to the modeling of the electromagnetic subsystem of the coupled process and report on its validation by a benchmark procedure. It is analysed which numerical techniques are best suited to solve certain problems arising in the simulation. In particular, the algorithmic implementation within SOFAR is compared to a well experienced FD-code (FELMEC) developed and maintained at the Institute of Electrical Machines, Drivers and Power Electronics. In addition, results from experiments carried out at the chair of forming at the university of Dortmund by Badelt et al. [3] and Beerwald et al. [4] serve as references.

2 Model Formulation of the Electromagnetic Subsystem

2.1 Derivation of Basic Equations

The state of an electrodynamic system is characterized by for vector fields \vec{E} , \vec{D} , \vec{B} , \vec{H} , fulfilling Maxwell's equations

$$\begin{aligned} \operatorname{div} \vec{D} &= \rho & \operatorname{div} \vec{B} &= 0 \\ \operatorname{curl} \vec{H} &= \vec{J} + \dot{\vec{D}} & \operatorname{curl} \vec{E} &= -\dot{\vec{B}}. \end{aligned} \quad (1)$$

Here \vec{J} denotes the conducting current and ρ the density of electric charges, which is zero in the given situation. Dots indicate total derivatives. In the realm of the quasistatic hypothesis, which applies to EF since the characteristic wave length of the electromagnetic field are much longer than the structure of interest, displacement currents $\dot{\vec{D}}$ are negligible (see e.g. [17] or [18]). The region Ω in which the forming process takes place consists of three parts, the workpiece \mathcal{W} , the tool coil \mathcal{S} and the space around workpiece and tool-coil. We assume that the respective materials possess linear isotropic polarization and magnetization with permittivity ε and permeability $\mu = \mu_0$ such that $\vec{B} = \mu\vec{H}$ and $\vec{D} = \varepsilon\vec{E}$ may be assumed throughout Ω within the scope of accuracy, where μ_0 denotes the permeability of the vacuum. We further assume that the tool coil remains stationary during the process such that \vec{B} equals the time derivative $\dot{\vec{B}} = \partial_t \vec{B}$ outside \mathcal{W} . If the workpiece moves at a velocity \vec{v} , we obtain $\dot{\vec{B}} = \partial_t \vec{B} + \text{curl}(\vec{v} \times \vec{B})$ inside \mathcal{W} . Finally, \vec{J} is related to the other fields by the constitutive equation

$$\vec{J} = \gamma \vec{E}. \quad (2)$$

Here, $\gamma = \gamma(\vec{x}, t)$ denotes the conductivity of the material at a point \vec{x} at time t . To solve Maxwell's equations, a vector potential \vec{A} and a scalar potential Φ are introduced. If \vec{A} and Φ fulfill the coupled equations

$$\begin{aligned} \text{curl} \frac{1}{\mu} \text{curl} \vec{A} + \gamma \partial_t \vec{A} - \gamma (\vec{v} \times \text{curl} \vec{A}) &= -\gamma \text{grad} \Phi \\ \Delta \Phi &= \text{div} \partial_t \vec{A} - \text{div} (\vec{v} \times \vec{B}), \end{aligned} \quad (3)$$

then $\vec{B} = \text{curl} \vec{A}$, $\vec{E} = \gamma (-\text{grad} \Phi - \partial_t \vec{A} + \vec{v} \times \vec{B})$, $\vec{D} = \varepsilon \vec{E}$, $\vec{H} = 1/\mu \vec{B}$ fulfill the quasistatic version of Maxwell's equation for linear isotropic materials in each part of the region Ω . Solutions to (3) need not to be continuous at interfaces between two materials. However, the components of \vec{B} and \vec{J} normal to the interface are continuous as well as the tangential components of \vec{E} . In the following, we assume that a Coulomb gauge condition $\text{div} \vec{A} = 0$ holds. If additionally $\text{div} (\vec{v} \times \vec{B}) = 0$ holds, equations (3) decouple. Both the Coulomb gauging and the latter condition are generally fulfilled for 2D problems or in the axisymmetric situation. Consequently, the second equation can be solved independent of \vec{A} and $\text{grad} \Phi$ can be inserted in the first one. In addition to equation (3), boundary conditions are necessary to determine \vec{A} and Φ : As before, Ω denotes the domain, in which a magnetic field distribution is to be computed and \mathcal{S} is the domain of a coil with (congruent) front surfaces \mathcal{F}_1 and \mathcal{F}_2 and a spiral lateral surface \mathcal{L} . Further, let the potential U_1 and U_2 be given on \mathcal{F}_1 and \mathcal{F}_2 respectively. As the area adjacent to \mathcal{S} possesses conductivity $\gamma = 0$, Φ solves on a stationary tool coil \mathcal{S} the equation

$$\begin{aligned} \Delta \Phi &= 0 & \text{in } \mathcal{S} & & \Phi &= U_1 & \text{on } \mathcal{F}_1 \\ \Phi &= U_2 & \text{on } \mathcal{F}_2 & & \partial_n \Phi &= 0 & \text{on } \mathcal{L}, \end{aligned} \quad (4)$$

where ∂_n denotes the derivative in direction of the outer normal. Outside \mathcal{S} we may assume $\Phi = 0$. Although there exists no boundary for \vec{A} , it is justified to restrict it to a bounded domain Ω and to assume that \vec{A} vanishes on its boundary, since $\vec{A}(\vec{x}) = O(1/|\vec{x}|^2)$ for $|\vec{x}| \rightarrow \infty$. If instead of the potential U on the front sides of the coil the total current $I = I(t)$ in the tool coil is known,

then the two equations (3) have to be tackled simultaneously, i.e. the system

$$\begin{aligned} \operatorname{curl} \frac{1}{\mu} \operatorname{curl} \vec{A} &= -\gamma \left(\partial_t \vec{A} + \operatorname{grad} \Phi - \vec{v} \times \operatorname{curl} \vec{A} \right) \quad \text{in } \Omega \\ \Delta \Phi &= 0 \quad \text{in } \mathcal{S} \quad \Phi = 0 \quad \text{in } \Omega \setminus \mathcal{S} \end{aligned} \quad (5)$$

has to be considered together with the afore mentioned boundary conditions for \vec{A} and Φ and with

$$-\gamma \int_{\mathcal{C}} \left(\partial_t \vec{A} + \operatorname{grad} \Phi \right) d\vec{a} = I \quad (6)$$

for any cross section \mathcal{C} parallel to \mathcal{F}_1 and \mathcal{F}_2 ($d\vec{a}$ = surface element).

2.2 The Axisymmetric Situation

Spiral coils as used for EF are not axisymmetric, but can be approximated in good accuracy by the following idealization: If \mathcal{S} consists of n windings, each winding is replaced by a torus of the same cross section \mathcal{C} . The resulting n tori are cut at an azimuthal angle of $\varphi = 0$. These cuts are considered as perfectly isolating. Next, the cross section at $\varphi = 0$ of each torus (except of the first one) is set on the same potential level as the cross section of the preceding torus at $\varphi = 2\pi$. If \mathcal{T}_k denotes the k th torus resulting from this process and U_k the potential of \mathcal{T}_k at $\varphi = 0$, then $\Phi = \Phi(r, \varphi, z)$ satisfies for $k = 1 \dots n$

$$\begin{aligned} \Delta \Phi &= 0 \quad \text{in } \mathcal{T}_k & \Phi &= U_k \quad \text{for } \varphi = 0 \quad (\text{in } \mathcal{T}_k) \\ \Phi &= U_{k+1} \quad \text{for } \varphi = 2\pi \quad (\text{in } \mathcal{T}_k) & \partial_n \Phi &= 0 \quad \text{on } \partial \mathcal{T}_k. \end{aligned} \quad (7)$$

Consequently, Φ possesses the form

$$\Phi(r, \varphi, z) = U_k + \delta U_k \frac{\varphi}{2\pi} \quad (8)$$

with $\delta U_k = U_{k+1} - U_k$. For the determination of

$$\nabla \Phi = \frac{\delta U_k}{2\pi r} \vec{e}_\varphi, \quad (9)$$

where \vec{e}_φ denotes a unit vector in azimuthal direction, only the potential differences δU_k need to be considered. They can be obtained from the measured total current $I = I(t)$ in the coil as follows: The average over all currents flowing through an arbitrary cross section \mathcal{C}_k through the k th torus amounts to

$$I = -\gamma \int_{\mathcal{C}_k} \left(\partial_t \vec{A} + \operatorname{grad} \Phi \right) d\vec{a} = -\gamma \int_{\mathcal{C}_k} \left(\partial_t \vec{A} + \frac{\delta U_k}{2\pi r} \vec{e}_\varphi \right) d\vec{a}. \quad (10)$$

From relation (10), δU_k can be determined:

$$\delta U_k \cdot \int_{\mathcal{C}_k} \frac{1}{2\pi r} \vec{e}_\varphi d\vec{a} = -\frac{I}{\gamma} - \int_{\mathcal{C}_k} \partial_t \vec{A} d\vec{a} \quad (11)$$

implying

$$\delta U_k = -2\pi \left(h \ln \frac{b_k}{a_k} \right)^{-1} \cdot \left(\frac{I}{\gamma} + \int_{\mathcal{C}_k} \partial_t \vec{A} d\vec{a} \right) \quad (12)$$

for a coil with rectangular cross section, where h is the height (= size in z -direction), a_k the inner and b_k the outer radius of the k th winding. Thus, we obtain

$$\nabla \times \frac{1}{\mu} \operatorname{curl} \vec{A} + \gamma \partial_t \vec{A} = \begin{cases} \left(r \cdot h \ln \frac{b_k}{a_k} \right)^{-1} \cdot \left(I + \gamma \int_{C_k} \partial_t \vec{A} da \right) & \text{in } \mathcal{S} \\ \vec{v} \times \operatorname{curl} \vec{A} & \text{in } \mathcal{W} \\ 0 & \text{in } \Omega \setminus (\mathcal{S} \cup \mathcal{W}). \end{cases} \quad (13)$$

The coefficients a_k and b_k in this equation depend on the spatial variable \vec{x} in so far as they assume a certain value depending on the coil winding in which \vec{x} is located.

3 Discussion of different Algorithmic Implementations

There exist several possibilities to model the electromagnetic subsystem. The finite element (FE) method offers a flexible method that can easily be adapted to changing demands and that offers various numerical algorithms that allow an optimized performance for a large scale of different problems. In particular, both the electromagnetic and the mechanical subsystem can be implemented in a single software environment which results in an enormous gain of performance. The latter is much more difficult with the FD method or the boundary element method due to their inherent restrictions. In addition, the FE method allows the use of unstructured meshes and adaptive refinement such that it can cope with singularities, problems having solutions with restricted regularity or other numerical difficulties. Thus the software environment SOFAR had been chosen for the development of a simulation tool for EF. On the other hand, complex computer code is susceptible for errors and thus a well experienced, clearly written code that serves as reference is desirable. For this purpose, the above mentioned FD code is applied.

3.1 Program Structure

Essential for an FE tool to be applied in research is its clear structure such that extensions and new algorithms can quickly be implemented. Such a structure can be reached by an object oriented design as done in SOFAR: The interface to the developer is implemented in JAVA. On the other hand, time critical jobs like basic linear algebra (BLAS-) operations are implemented in fast native C and FORTRAN Code. Unstructured meshes which are typical for adaptive refinement and remeshing strategies can easily be handled. In particular, SOFAR administrates geometric singularities as e.g. hanging nodes. The assembly of the corresponding stiffness matrices is done automatically. Moreover, SOFAR allows access to any geometric substructure of a particular finite element like edges or faces. The latter enables easy implementation of edge elements which are used for 3D electrodynamical problems [19, 20]. Moreover, effective algorithms like multigrid solver or error estimators are available. SOFAR can be extended by external routines (written in C or FORTRAN) due to a user interface. This user interface was e.g. applied for the implementation of structural mechanic finite elements developed at the chair of Mechanics at the University of Dortmund.

3.2 Design of suitable Meshes

One has to decide whether the whole coupled problem is treated in one mesh or if each subsystem is simulated in a mesh of its own. The first approach offers the advantage that a consistent linearization of the coupled non linear equation can easier be implemented. On the other hand coefficients of largely differing magnitude within the common stiffness matrix lead to largely differing eigenvalues and thus probably disturb the stability of the method. Moreover, the numerically sensitive parts of the electrodynamic and the mechanical subsystem are localized in different spatial areas. A treatment in different meshes allows to adapt the particular mesh by local refinement. Consequently, electromagnetic and mechanical subsystem are simulated in different meshes in case of the SOFAR simulation.

It is *natural* that the mechanical mesh moves with the structure. Whether the electromagnetic mesh should rest or move is a difficult question: A moving electromagnetic mesh, representing the Lagrangian point of view offers two advantages: First, data exchange between the structure mesh and the electromagnetic mesh is easier, because node-oriented data can be transferred without rearrangement. Second, the convective term $\vec{v} \times \text{curl } \vec{A}$ need not to be considered explicitly if the time derivative $\partial_t \vec{A}$ is replaced by the total derivative $\dot{\vec{A}}$ in (13) (see [18]), since

$$\dot{\vec{A}} = \partial_t \vec{A} + \text{grad}_{\vec{A}} (\vec{v} \cdot \vec{A}) - \vec{v} \times \text{curl } \vec{A}. \quad (14)$$

The term $\text{grad}_{\vec{A}} (\vec{v} \cdot \vec{A})$ disappears if \vec{v} and \vec{A} are perpendicular which is the case for all 2D or axisymmetric problems. In a moving mesh, $\dot{\vec{A}}$ is simply obtained by considering corresponding nodal values of two subsequent meshes. On the other hand, a fixed mesh, representing an Eulerian approach, avoids global remeshing in every time step. Then $\vec{v} \times \text{curl } \vec{A}$ has to be considered in the weak form of (13). As the Péclet-number

$$P_e = \frac{\mu\gamma|\vec{v}|h}{2} \approx 0.5 \quad (15)$$

is small in the given situation, the stability of the numerical solution process is not affected. The circumstance that the resulting stiffness matrices are no longer symmetric such that (preconditioned) conjugate gradient solvers cannot be applied is of minor importance, as SOFAR is equipped with a BICGSTAB solver that can treat the corresponding linear equations effectively. Moreover a fixed mesh reduces the expenses for the accumulation of the stiffness matrix because only part of it needs to be reassembled. While the electromagnetic field calculation in SOFAR works on a fixed mesh, the FD method uses a moving one. A detailed comparison of the performance and accuracy of these two approaches represents work in progress.

3.3 Finite Element Formulation

While a standard finite element approach with so called nodal elements is applicable for 2D problems or problems with certain symmetries, numerical field computation in 3D requires a more sophisticated approach. Therefore, Nédélec introduced edge elements in 1980 and 1986 [19, 20]. Here the degrees of freedom that have to be determined are not nodal values of \vec{A} but integrals over \vec{A} along the edges of the discretizing mesh. These elements simulate the typical jumps, solutions to Maxwell's equations exhibit at interfaces between different materials

and, hence, avoid locking and spurious modes. As the benchmark problem considered below is formulated for an axisymmetric situation, nodal elements with four nodes are applied.

We derive now the weak form of equation (13) and its discretization in the axisymmetric situation, which is the basis of the FE simulation. If A_φ denotes the azimuthal component of \vec{A} and r the radial component of a point and z its axial component then (13) is equivalent to

$$\begin{aligned} \frac{1}{\mu} \int_{\Omega} \left(r (\partial_r A_\varphi \partial_r A^* + \partial_z A_\varphi \partial_z A^*) + \frac{A_\varphi A^*}{r} \right) - \gamma \int_{\mathcal{W}} \left(v_r \partial_r A_\varphi + v_z \partial_z A_\varphi + \frac{v_r A_\varphi}{r} \right) A^* \\ + \gamma \int_{\Omega} \partial_t A_\varphi A^* = \begin{cases} \int_{\mathcal{S}} r \left(h \ln \frac{b_k}{a_k} \right)^{-1} \cdot \left(I + \gamma \int_{\mathcal{C}_k} \partial_t A_\varphi \right) \cdot A^* & \text{in } \mathcal{S} \\ 0 & \text{in } \Omega \setminus \mathcal{S} \end{cases} \end{aligned}$$

for all test functions $A^* \in H^1$ that decay sufficiently fast for $r \rightarrow 0$. In all integrals, the integration has to be carried out with respect to $drdz$. Inserting the FE basis representation of A_φ and A^* we obtain a linear system of equations. The first integral leads to the permeability matrix K , the third to the conductivity matrix B and the second to an unsymmetric matrix C representing the convective part. Since the source vector $\vec{f} = \vec{f}(\vec{a})$ is a function of \vec{a} the resulting equation

$$K\vec{a} + C\vec{a} + B\dot{\vec{a}} = \vec{f}(\vec{a}) \quad (16)$$

has to be solved iteratively. This can be avoided by discretization of $\int_{\mathcal{C}_k} \partial_t A_\varphi$ and adding the resulting linear equations to the stiffness matrix. But the management of the additional coupling of degrees of freedom, that are not linked to each other by a neighbor relation, is more expensive than the implementation of the iterative scheme. Moreover, in each iteration step only $f(\vec{a})$ has to be reassembled such that numerical costs remain small. Benchmark tests have shown that this methods exhibits satisfactory performance.

3.4 Finite-Difference Approach

The Finite-Difference method is usually restricted to structured orthogonal grids. However, a generalization to nonstructured meshes including triangular and nonrectangular quadrangular cells is possible. The arising methods, one of which is applied in the inhouse FD-code FELMEC, are e.g. referred to as Box-Techniques, the resulting difference schemes of which are closely related to schemes based on Finite Elements [21].

The method used here is based on a modified vector potential $\Psi' = r \cdot A_\varphi$ for axisymmetric arrangements and described in [22, 23]. The values of Ψ' on the nodes are the primary unknowns of interest. In order to compute them, for each time step a system of linear equations is set up by evaluating Ampere's law for each node on a path through the grid cells adjacent to the node under consideration.

It should be mentioned that the values of the nodal amperage I_0 are not prescribed as external quantities, but are themselves unknown in workpiece and tool coil. For nodes in free space they are zero anyway, whereas for the tool coil cross-section I_0 is replaced by an expression including the time derivative of Ψ'_0 and the external driving voltage u_{ex} along the winding turn under consideration. All winding turns are also regarded as branch elements of a network, for which Kirchhoff's laws are applied. The prescribed current i of the tool coil is given by a current source. The necessary voltage-current relations of the windung turns are set up

as a summation of the nodal amperages I_0 on the winding cross-section. The resulting overall system of equations is solved directly for each time step.

In contrast to [23], where the coupling of the moving structure to the orthogonal base grid is carried out by an interpolation strategy leaving the original base grid unaltered, here a remeshing procedure is applied. First, all grid cells of the base grid, which are totally or partially covered by the workpiece, as well as cells with nodes lying too close to the workpiece mesh are deactivated. Hence, an interior boundary in the base grid occurs. Then, the exterior workpiece contour and the resulting interior base grid contour are linked by triangular cells forming a coherent mesh. Here, additional triangular cells occur, whenever nodes of the interior base grid contour are connected diagonally. In order to ensure that all nodes of the original workpiece mesh are adjacent to four quadrangular grid cells, an extended workpiece mesh with an additional layer of nonconductive grid cells is used for the procedure described above. The topology regularized by this mesh extension is considered advantageous for the computation of nodal forces by evaluating Maxwell's stress tensor. Figure 1 shows a detail of a mesh generated for a workpiece geometry at $63 \mu\text{s}$, which resulted from the staggered EMAS-MARC coupling presented in [9]. As pointed out before, the coefficients for the generalized FD-scheme or Box-

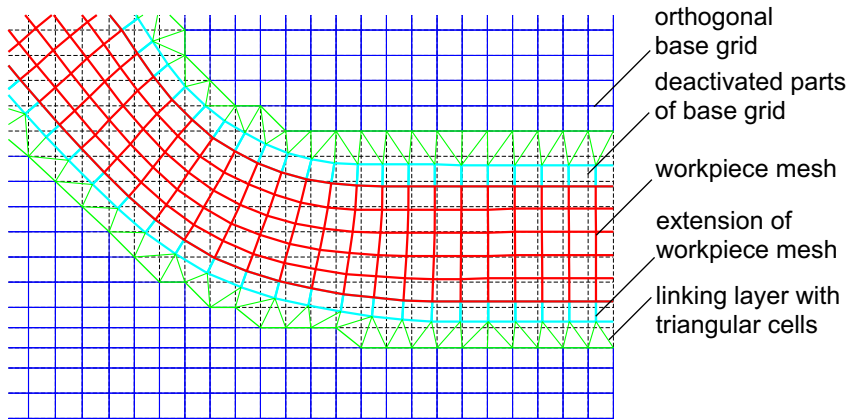


Figure 1: Detail from remeshed Finite-Difference grid showing the workpiece mesh, its non-conductive extension and the linking layer to the remaining active base grid.

scheme can be derived in quite the same way as in the basic orthogonal grid by evaluating Ampere's law. In order to obtain expressions for the magnetic field strength in a triangular cell depending on the nodal values of Ψ' , a linear approximation for Ψ' in z and r^2 in the triangle is chosen:

$$\Psi'(r, z) = c_0 + c_r r^2 + c_z z. \quad (17)$$

The constants c_0 , c_r and c_z are computable in dependence on the three nodal values Ψ'_I , Ψ'_{II} and Ψ'_{III} by solving a linear system of equations. The coefficients c_r and c_z are related to the flux density components in the triangular cell as a result of $\vec{B} = \text{curl } \vec{A}$:

$$B_z = 2c_r, \quad B_r(r) = -\frac{c_z}{r}. \quad (18)$$

The contribution to the circulation of the magnetic field around a node under consideration, which results from the part of the integrational path through the triangle from one edge to

another according to Fig. 2, can be calculated as follows:

$$\int_{M_{I,II}}^{M_{I,III}} \vec{H} d\vec{l} = \frac{1}{\mu} \int_{M_{I,II}}^{M_{I,III}} \left(-c_z \frac{dr}{r} + 2c_r dz \right). \quad (19)$$

Since it does not depend on the path itself due to $\text{curl } \vec{B} = 0$ for the field in (18) and $\mu = \text{const.}$

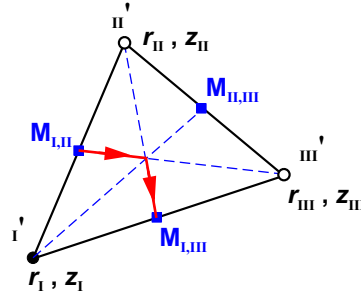


Figure 2: Triangular cell with nodes I, II and III, edge median points $M_{I,II}$, $M_{II,III}$ and $M_{I,III}$ and part of integrational path (arrows) surrounding node under consideration, here No. I, along median lines.

inside the cell, simply a parametrized straight line can be assumed for evaluating (19). The constants c_r and c_z are replaced by the nodal values of Ψ' . Finally, a linear combination of these modified nodal vector potentials is obtained:

$$\int_{M_{I,II}}^{M_{I,III}} \vec{H} d\vec{l} = \alpha_{I,II} \Psi'_{II} + \alpha_{I,III} \Psi'_{III} - (\alpha_{I,II} + \alpha_{I,III}) \Psi'_{I}. \quad (20)$$

Here, e.g. the coefficient $\alpha_{I,II}$ is given by

$$\alpha_{I,II} = \frac{1}{\mu \Delta} \left((z_{III} - z_I)(z_{III} - z_{II}) + (r_{III}^2 - r_I^2) \ln \frac{r_{III} + r_I}{r_{II} + r_I} \right) \quad (21)$$

and Δ stands for

$$\Delta = (r_{II}^2 - r_I^2) (z_{III} - z_I) - (r_{III}^2 - r_I^2) (z_{II} - z_I). \quad (22)$$

The logarithmic expression in $\alpha_{I,II}$ results from integrating the $1/r$ -dependence. However, it can be shown that for large radii and comparably low radial distances of the nodes the coefficients α become approximately those expressions, which are obtained in rectangular coordinates (2D problems) for first order finite elements.

The quadrangular grid cells in the workpiece are treated in a similar way based on a subdivision of such a cell into four underlying triangles. The modified vector potential Ψ'_c of the center point as the point in common for the four triangles is assumed to be a linear combination of the values $\Psi'_{1...4}$ of the quadrangle's vertices with weighting coefficients $\kappa_{1...4}$ depending on geometry and their sum equaling one. The paths of integration are led from the edge median points to the center point right through the adjacent triangle. The according contribution to the magnetic circulation under consideration depends on Ψ'_c as well as on two vertex potentials. After replacing Ψ'_c by the aforementioned linear combination only the vertex potentials occur and the resulting coefficients for matrix assembly are obtained.

In contrast to the base grid, where matrix assembly is carried out row by row, i.e. nodal

equation by nodal equation, for the nonorthogonal parts of the mesh the matrix is assembled by adding the contributions e.g. arising from (21) to the coefficient matrix grid cell by grid cell, similar to matrix assembly in the Finite Element Method.

3.5 Timestepping

As time stepping for the electromagnetic subsystem the generalized trapezoidal rule has been chosen. Only the conductivity matrix B and the convective matrix C have to be reassembled in every time step, while the permeability matrix K does not change due to the choice of a fixed mesh. At the beginning of the process vibration due to the switching on of power have to be filtered out. Consequently the parameter of the generalized trapezoidal rule has to be chosen close to the backward Euler situation. Later, the optimal parameter yielding an accuracy of $O(\delta_t^2)$ can be chosen, where δ_t is the size of the time step.

In the FD-code the same method also known as θ -method is applied. According to the following approximation of integrals of a quantity $q(t)$ over one time step

$$\int_t^{t+\delta_t} q(\tau) d\tau = (1 - \theta)\delta_t q_{t+\delta_t} + \theta\delta_t q_t, \quad (23)$$

$\theta = 0$ results in the backward Euler formula, whereas $\theta = 0.5$ is the mere trapezoidal rule. For the computations carried out here for θ a value of about a third has been chosen sometimes referred to as Galerkin approach. A moving mesh is used, so that the convective term does not occur explicitly. All contributions to electromagnetic induction, motion conditioned as well as arising from field variation, are included by evaluating the total derivative of the nodal modified vector potentials Ψ' . However, the reluctance matrix has to be regenerated in every time step.

3.6 Coupling Strategies

The coupling between the two subsystems is carried out in a staggered way. This means that the magnetic field distribution is calculated with respect to the position and velocity of the structure in the n th time step. After that the new position of the structure is determined such that a balance between inner and outer forces arises. However, benchmark simulation have shown that this algorithm can be improved by adding an additional iteration loop: To ensure that the computed momentum balance of the structure in the $(n + 1)$ st time step represents a balance between the Lorentz forces in the $(n + 1)$ st time step and the inner forces of the structure at this instant, the following scheme is applied: Let all values having index n be variables of the n th time step. Then the update for the $(n + 1)$ st time step looks like this:

1. A predictor value $\vec{A}_1^{(n+1)}$ for the vector potential and for its time derivative in the $(n + 1)$ st step is computed according to the measured amperage in the tool coil at time $t^{(n+1)}$ and the kinematic state of the workpiece. For this, the assembly routine of the magnetic mesh checks whether a certain point lies in the workpiece or not. The values for conductivity and for the velocity of the structure are chosen respectively.
2. The stiffness matrix and load vector in the workpiece mesh are assembled. For this, the nodal values of the current Lorentz force density are computed according to

$$f_L^{(n+1)} = \vec{J}_1^{(n+1)} \times \vec{B}_1^{(n+1)} = \gamma \partial_t \vec{A}_1^{(n+1)} \times \text{curl} \vec{A}_1^{(n+1)}. \quad (24)$$

3. The assembled equation in the workpiece mesh is solved. The computed deformations are added to the vertex positions of the workpiece mesh. It is checked, whether the residual force associated with the resulting state of deformation is zero in the scope of desired accuracy. If the latter is false, another step of the Newton-Raphson iteration has to be performed with the altered position of the workpiece. Otherwise, the vector potential $\vec{A}_2^{(n+1)}$ according to the new kinematic state of the structure is computed. If it does not deviate from $\vec{A}_1^{(n+1)}$ within the scope of accuracy, the next time step is started. Otherwise, the equilibrium position of the structure with respect to outer forces resulting from $\vec{A}_2^{(n+1)}$ and its time derivative is determined.
4. A series of vector potentials $\vec{A}_k^{(n+1)}$ and corresponding equilibrium positions of the mechanical structure is computed, until $\vec{A}_{k+1}^{(n+1)} = \vec{A}_k^{(n+1)}$ within the scope of accuracy. Then a new time step is started.

Using the Finite-Difference code FELMEC for the electromagnetic subsystem one can set up an explicit coupling scheme, the accuracy of which is considered sufficient, if a small time step of e.g. 0.1 ... 0.2 μs is chosen. Having calculated the nodal forces in the workpiece the electromagnetic simulation has to be interrupted after each time step. The calculation of nodal forces is carried out by a local evaluation of Maxwell's stress tensor on a surface around a node under consideration. The list of nodal forces is written out and passed to the structural mechanical part of SOFAR as a prescribed load, which calculates an update of the workpiece shape and mesh. With this updated mesh the electromagnetic computation is continued. Control and synchronization of the two processes are carried out by a shell script and JAVA-routines in SOFAR.

4 Validation by Benchmark Problems

Details of the implementation of the coupled electromagnetic field computation described above have been validated by several benchmark simulations involving comparisons with the programs EMAS, FEMM and ANSYS. The mechanical side has been tested in [16]. Here we present a benchmark test that allows to validate the fully coupled simulation, where the above described FD-code serves as reference. Although many questions have already been clarified, the benchmark process and the optimization of SOFAR are still work in progress.

To validate whether SOFAR computes a correct force distribution, first a fully coupled simulation is carried out with SOFAR. Thereby the same geometry and input currency are regarded as described in [16]. In particular, the mechanical side is simulated by an elastoplastic element. Although this modeling fails to account for the rate dependency of the mechanical structure it suffices for a validation of the electromagnetic field computation as it leads to approximately correct results (see [16] or [1, 2, 3, 9]). Next, the FD-code is coupled with SOFAR such that the computation of the electromagnetic field is carried out by the FD-Software, while SOFAR simulates the mechanical subsystem. The results of these simulations are compared to each other and to experimental results. Both simulations mirror the forming process qualitatively correctly: Figure 3 shows the shape of the work piece after 35 μs . The form of the work piece stays extremely similar during the whole forming process in both simulations. This

shows that both approaches, although completely different, are basically numerically equivalent for this example. Moreover, comparison to experimental data from [3, 4] shows that the

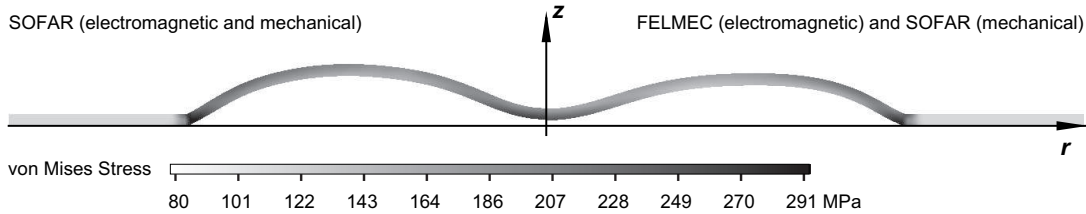


Figure 3: Workpiece contour and von Mises stress at instant of time $t = 35 \mu\text{s}$

coupling of SOFAR with the FD-code leads to a satisfactory result*: Figure 4 shows the vertical displacement of the structure on the axis and at a radius of 21 mm for both simulations in comparison with experimental data. However, with the current parameters, SOFAR computes

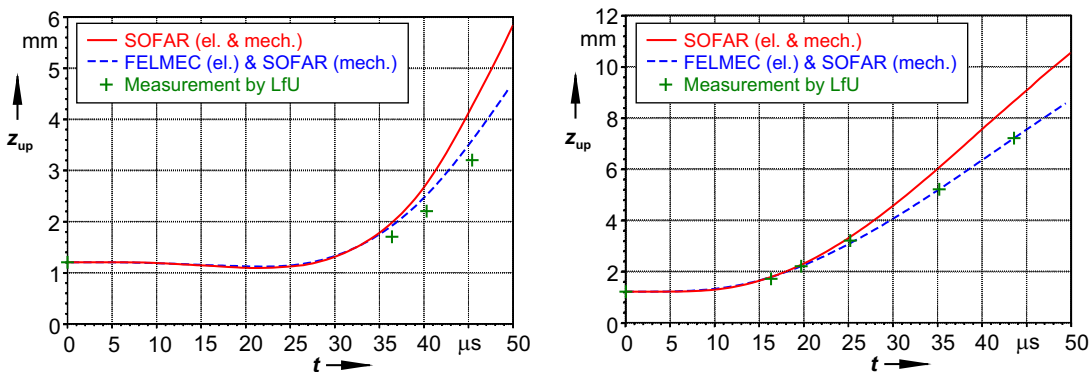


Figure 4: Position of upper workpiece surface on axis $r = 0 \text{ mm}$, graph on left hand side, and at $r = 21 \text{ mm}$, graph on right hand side.

a slightly larger distribution of forces than the FD-simulation leading to more deformation of the work piece. In the beginning, both simulations yield nearly the same displacement but after 35 and 20 μs respectively the deviation becomes obvious achieving a value of about 2 mm after 60 μs . This deviation is mainly caused by the different spatial discretizations used for electromagnetic field computation (up to 47000 unknowns in the case of the FD-SOFAR simulation and 1126 unknowns for the SOFAR computation). The results of the simulation show that the discretization within SOFAR has been chosen much too coarse. To increase the accuracy of SOFAR without reducing its efficiency, adaptive meshing algorithms based on local error estimation will be implemented soon. Moreover, the choice of optimal numerical parameters is still work in progress and will be carried out with the help of further benchmark tests.

5 Conclusions

The algorithmic implementation of the electromagnetic subsystem of a fully coupled simulation tool for electromagnetic forming has been presented. Details of the realization of the underlying physical model are discussed. In particular, the tool coil is correctly modeled as massive

*Note that an elastoplastic model slightly overestimates the deformation of the workpiece (see e.g. [16]).

conductor with the help of an iterative scheme. Convective terms are accounted within the weak form of the field equations. The non linear coupling between the magnetical and mechanical subsystem is performed in a staggered but implicit way, allowing for larger time steps. The applied algorithms have been tested and optimized with the help of suitable benchmark tests. Although SOFAR can in principle cope with the computation of the Lorentz force distribution coupling the electromagnetic system and the mechanical structure, further improvements concerning the accuracy of the field computation are necessary to obtain full accordance to experimental data. In particular, numerical algorithms for error control and adaptive refinement have to be implemented and validated by further benchmark simulations. This will improve SOFAR to a convenient and reliable tool for the simulation of EF forming processes.

References

- [1] C. Beerwald, A. Brosius, W. Homberg, M. Kleiner, and A. Wellendorf. New aspects of electromagnetic forming. In *Proceedings of the 6th International Conference on the Technology of Plasticity*, volume III, pages 2471–2476, 1999.
- [2] C. Beerwald, A. Brosius, and M. Kleiner. Determination of flow stress at very high strain-rates by a combination of magnetic forming and fem calculation. In *Proceedings of the International Workshop on Friction and Flow Stress in Cutting and Forming (CIRP)*. ENSAM - Paris, 2000.
- [3] M. Badelt, C. Beerwald, A. Brosius, and M. Kleiner. Process analysis of electromagnetic sheet metal forming by online-measurement and finite element simulation. In *Proceedings of the 6th International ESAFORM Conference on Material Forming*, 28.-30. April 2003, Italy, pages 123–126. ESAFORM 2003, 2003.
- [4] C. Beerwald, A. Brosius, M. Kleiner, and V. Psyk. Einfluss des magnetischen Druckes bei der elektromagnetischen Blechumformung. In *2. Kolloquium Elektromagnetische Umformung*. Forschergruppe “Untersuchung der Wirkmechanismen der elektromagnetischen Blechumformung”, 2003.
- [5] W. H. Gourdin. Analysis and assessment of electromagnetic ring expansion as a high-strain rate test. *J. Appl. Phys.*, 65:411, 1989.
- [6] W. H. Gourdin, S. L. Weinland, and R. M. Boling. Development of the electromagnetically-launched expanding ring as a high strain-rate test. *Rev. Sci. Instrum.*, 60:427, 1989.
- [7] N. Takata, M. Kato, K. Sato, and T. Tobe. High-speed forming of metal sheets by electromagnetic forces. *Japan Soc. Mech. Eng. Int. J.*, 31:142, 1988.
- [8] G. Fenton and G. S. Daehn. Modeling of electromagnetically formed sheet metal. *J. Mat. Process. Tech.*, 75:6–16, 1998.
- [9] C. Beerwald, A. Brosius, W. Homberg, M. Kleiner, M. Klocke, and S. Kulig. Extended finite element modelling of electromagnetic forming. In *Proceedings of the 10th International Conference*, 14.-16. April 2003, United Kingdom, pages 559–566. SheetMetal 2003, 2003.
- [10] B. Svendsen and T. Chanda. Continuum thermodynamic modeling and simulation of electromagnetic forming. *Technische Mechanik*, 23:103–112, 2003.
- [11] B. Svendsen and T. Chanda. Continuum thermodynamic formulation of models for electromagnetic thermoinelastic materials with application to electromagnetic metal forming. *Cont. Mech. Thermodyn.*, 2004. submitted.

- [12] A. Brosius, M. Kleiner, and B. Svendsen. Finite-element modeling and simulation of the material behaviour and structural behaviour during electromagnetic metal forming of metal tubes and sheet metal. 2003. in preparation.
- [13] A. Brosius, T. Chanda, M. Kleiner, and T. Svendsen. Finite-element modeling and simulation of material behavior during electromagnetic metal forming. In *Proceedings of the 6th International ESAFORM Conference on Material Forming 28.-30. April 2003, Italy*, pages 971–974. ESAFORM 2003, 2003.
- [14] M. Stiemer, J. Unger, H. Blum, and B. Svendsen. Algorithmic formulation and numerical implementation of coupled multifield models for electromagnetic metal forming simulations. 2004. in preparation.
- [15] H. Blum, H. Kleemann, A. Rademacher, T. Rauscher, A. Schroeder, and M. Stiemer. SO-FAR. www.mathematik.uni-dortmund.de/lxx/sofar, 2003.
- [16] M. Kleiner, A. Brosius, H. Blum, F. T. Suttmeier, M. Stiemer, B. Svendsen, J. Unger, and S. Reese. Benchmark problems for coupled electromagnetic-mechanical metal forming processes. *Annalen der wissenschaftlichen Gesellschaft für Produktionstechnik*, 2004. in press.
- [17] F. Moon. *Magnetic interactions in solids*. Springer-Verlag, 1980.
- [18] M. Schinnerl, J. Schöberl, M. Kaltenbacher, and R. Lerch. Multigrid methods for the 3d simulation of nonlinear magneto-mechanical systems. *IEEE transactions magnetics*, 38:1497–1511, 2002.
- [19] J. C. Nédélec. Mixed finite elements in \mathbb{R}^3 . *Numerische Mathematik*, 35:315–341, 1980.
- [20] J. C. Nédélec. A new family of mixed finite elements in \mathbb{R}^3 . *Numerische Mathematik*, 50:57–81, 1986.
- [21] Ch. Großmann and H.-G. Roos. *Numerik partieller Differentialgleichungen*. Teubner Studienbücher-Mathematik, Stuttgart, 1994.
- [22] S. Kulig, M. Klocke, A. Joswig, D. Peier, and M. Hinck. Modellierung und Simulation der nichtlinearen elektromagnetischen kopplung zwischen Werkstück und Umformspule. In *Kolloquium elektromagnetische Umformung 2003*, 2003.
- [23] M. Klocke. Computation of axisymmetric transient electromagnetic fields by finite-difference schemes including prescribed motion. In *6. International Symposium on Electric and Magnetic Fields (EMF) 2003*, 2003.